In-operando dynamic visualization of flow through porous preforms based on X-ray phase contrast imaging

Teixidó, Helena; Caglar, Baris; Revol, Vincent; Michaud, Véronique

In-operando dynamic visualization of flow through porous preforms based on X-ray phase contrast imaging

Helena Teixidó [a], Baris Caglar [a,b], Vincent Revol [c], Véronique Michaud [a,*]

[a] Laboratory for Processing of Advanced Composites (LPAC), Institute of Materials (IMX), Ecole Polytechnique Fédérale de Lausanne (EPFL), Station 12, 1015 Lausanne, Switzerland
[b] Aerospace Manufacturing Technologies, Faculty of Aerospace Engineering, Delft University of Technology, Kluyverweg 1, Delft 2629HS, Netherlands
[c] CSEM SA, Untere Gründlistrasse 1, 6055 Alpnach, Switzerland

ABSTRACT

Direct visualization is often sought to elucidate flow patterns and validate models to predict the filling kinetics during processes whereby a liquid resin infiltrates a textile porous preform. Here, X-ray phase contrast interferometry is evaluated to image in-operando constant flow rate impregnation experiments of a model fluid into glass, carbon and flax fabrics and a 3D printed structure. A methodology is presented to build the dynamic saturation curve based on image analysis of the dark field images, in which the pixel intensity values are transformed into saturation level versus position and time. The results prove the suitability of this technique to observe the progressive saturation averaged through the thickness of translucent and non-translucent preforms. The porosity network formed by the layers of fabric, the refractive properties of the material, the fabric geometry and its position relative to the X-ray setup are reported to be the main parameters affecting image contrast.

1. Introduction

In Liquid Composite Molding (LCM) techniques, a resin is forced to flow through the open pore space of a fibrous reinforcement placed inside a mold. This filling step is crucial and should be adequately controlled, otherwise, entrapped air in the form of voids or unfilled areas may appear and detrimentally affect the final part properties. The saturation S of the fluid phase in the porous media is commonly defined as

$$S = \frac{V_l}{(1 - V_f)} \qquad (1)$$

where V_l is the injected liquid volume and $(1 - V_f)$ the total pore of the porous medium. The value of S varies between 0 and 1, corresponding to fully dry and wet states respectively. Textiles used in composite processing generally present a bimodal pore distribution leading to a dual scale flow during impregnation which is in turn linked to void formation inside the composite [1–7]. Fluid driven by viscous forces preferentially fills the *meso*-spaces in between the tows and in consequence, micro-voids are created inside the tows. Conversely, fluid driven by capillary wicking fills the micro-spaces inside the tows and in this case, *meso*-voids remain trapped in between the tows. As a result,

the porous reinforcement is progressively saturated and a competition between viscous and capillary forces takes place at the flow front. The ratio between viscous and capillary forces can be defined with the non-dimensional capillary number:

$$Ca = \frac{u_l \eta}{\gamma} \qquad (2)$$

where u_l, η and γ are respectively, the fluid velocity, viscosity and surface tension. The amount of voids is minimal when viscous and capillary effects compensate each other corresponding to an optimal capillary number Ca_{opt} which depends on the chosen fluid/fabric system [1,8].

Multiphase flow and progressive saturation of the preform have been extensively studied with the aim to accurately predict flow kinetics and produce fully impregnated parts without defects [1,2,8–20]. In practice, an in-situ observation of the flow is usually coupled to mathematical models and numerical simulations to predict unsaturated flows and void formation mechanisms. For simplicity, fluid flow is often modelled assuming that the liquid moves with a fully saturated front (also called "slug-flow"). In this case, capillary effects at the flow front are lumped in the conventional fluid flow equations as a pressure difference acting as a boundary condition at the flow front, called the capillary pressure drop

Table 1
Properties of fibrous reinforcements.

Fiber type	Structure	Fabric name	Areal weight [g/m²]	Fiber density [g/cm³]	Fiber diameter[μm]	Supplier
E-glass	2 × 2 twill	Twill Glass	390	2.6	9	Suter Kunststoffe AG
Carbon	Unidirectional	UD Carbon	270	1.8	7	Suter Kunststoffe AG
Flax	2 × 2 twill	Twill Flax	300	1.3	20 – 40	Bcomp
Flax	Unidirectional	UD Carbon	150	1.3	20 – 40	Bcomp

[21–23]. However, many deviations have been found in literature from this fully saturated state with a nonlinear pressure profile along the infiltrated length [2,17,24–28]. Therefore, two main strategies are commonly adopted to tackle unsaturated flow phenomena in composite processing. The first approach is based on soil science and multi-phase flow equations for porous media, which require the knowledge of saturation as a function of pressure, known in soil science as the imbibition-drainage curve, and relative and saturated permeability [9,17,19,25]. The second approach considers the preform as a dual-scale body, separating the intra- and inter-bundle impregnations and introducing a sink term into fully saturated models. Bundles are thus gradually filled and resin flow is treated as a double-slug flow phenomena [12,17,24,29].

Several experimental methods have been proposed for the visualization of flow front behavior to monitor the progressive saturation of the preform. In particular, many techniques exist to observe the flow through glass preforms taking advantage of its translucency compared to fabrics made out of carbon. The most common and simple method is an optical observation of the impregnation with a camera or a microscope followed by an image analysis to extract the flow front information [3,9,30,31]. In order to improve the flow front traceability, some researchers used fluorescent dyes to increase the contrast between the fluid and the fabric [32–34]. For the same purpose, Gascón et al. [18,19] and LeBel et al. [35] proposed a method based on Visible Light Transmission (VLT) coupled with a 2D tomographic reconstruction. The saturation curves are thereafter built from an image analysis of the video frames or image acquisitions. Nevertheless, the accuracy of those optical techniques to extrapolate the saturation along the thickness is limited when several layers of fabric are used and they are only suitable for translucent preforms. Besides, when few layers are used wall effects between the fabric and the mold are more prominent and the observed flow pattern might not be an ideal representation of the reality (e.g. nesting between layers and change in porous network due to compression are not taken into account) [36,37]. Recently, Caglar et al. [38] proposed a novel method to assess the role of capillary effects by rapidly curing of the resin by UV-initiation during impregnation and analyzing the flow front after flow has stopped. Other methodologies were also proposed to extract the flow saturation without directly visualizing the flow. For example, Villière et al. [39] found that heat transfer is very sensitive to saturation and thus developed an experimental protocol based on tracking heat transfer with heat flux sensors coupled to a mathematical model to find the saturation curve for glass fabrics. Gueroult et al. [40] and Carlone et al. [41,42] used dielectric sensors to monitor the filling of a non-conductive glass preform by measuring the capacitance variations induced by the fluid movement.

It is noteworthy that infiltration has been seldom observed for non-translucent and electrically conductive fabrics such as carbon. Endruweit et al. [43,44] used Magnetic Resonance Imaging (MRI) to map the fluid distribution at the *meso*-scale in glass and carbon fabrics. However, two main drawbacks were pointed out: scanning periods were between 7 and 20 min (too long compared to impregnation speeds) and the spatial resolution was limited by signal relaxation effects. Ravey et al. [45] were able to obtain a good tracking of the flow front position of glass and carbon fabrics during wicking experiments with Infrared Thermography (IRT) but this technique is limited to single plies. Lystrup et al. [46] proposed a method based on fluorescent dyes to carry out in-situ optical

observations of a carbon reinforcement infusion to study void formation mechanisms. However, this method is again restricted to rather thin samples, and introduces the risk of dye particles filtering and changes in the wetting of the modified fluid. Recently, X-ray Computed Tomography (XCT) has been proposed for observation of in-situ transport phenomena due to its high spatial resolution at microscopic level and its versatility in terms of materials observed [47,48]. Despite the low temporal resolution of this technique, some researchers [49–51] were able to use XCT acquisition times of around two minutes using synchrotron radiation on small scale samples. In spite of the interest in the field, there is still a need of precise and reliable time-resolved experimental tools for the direct observation of the fluid flow through the open pore space of industry-relevant systems.

A novel technique called X-ray phase contrast has been developed over the last twenty years and combines a standard X-ray tube and gratings [52–57]. The concept is based on creating an interference pattern which is modified when an object is placed in between the X-ray source and the gratings. The resulting phase modulation is thus transformed into an intensity modulation and the changes in the intensity pattern with and without sample are exploited to recognize the small and ultra-small angle scattering quantified and represented as dark field (or scattering) images. This system is very sensitive to inhomogeneities inside a sample on a scale smaller than the image resolution and is thus convenient to observe materials with similar absorption and refraction properties but different microscopic internal structures. Even if this technique has mainly been applied in the medical field for static imaging [58,59], attempts of observing the distribution of a liquid into a solid material have been carried out by Yang et al. [60] and Prade et al. [61] who were able to visualize unsaturated water transport in mortar. In the case of composites, X-ray phase contrast has been used as a static non-destructive technique to visualize micro-cracks or pores in composites where usual X-ray absorption images do not show enough contrast [62–71]. Furthermore, this technique allows to detect microstructure variations of size comparable to the resolution of high resolution computed tomography with the advantage that larger samples can be observed and it can be adapted to conventional X-ray laboratory sources instead of synchrotron sources [72–74]. Therefore, the contrast between materials that present similar densities is greatly enhanced and images with thickness averaged microscopic precision could in principle be obtained with high spatial and time resolution with exposure times in the order of seconds [57,61].

We thus propose an in-operando experimental method based on X-ray phase contrast imaging for the visualization of fluid flow through translucent and non-translucent textile preforms using standard test fluids, at an image acquisition rate of a few seconds. After validating this novel method through flow experiments with translucent glass fiber fabrics against traditional video imaging methods, we assess the thickness-averaged flow evolution in non-translucent carbon fabrics. We vary impregnation conditions through the imposed flow rate, the number of layers and the volume fraction, analyze the resulting effect on image contrast and resolution, and develop a methodology to build the saturation curve from the grayscale analysis of the resulting images. Finally, we discuss the potential and limits of the method towards the study of impregnation of natural fibers and a polymeric pore network produced by 3D printing.
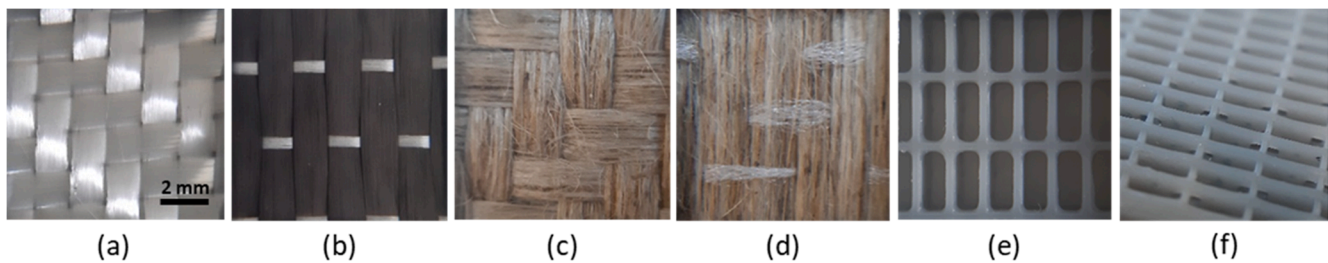
Fig. 1. Porous media: (a) twill glass, (b) UD carbon, (c) twill flax, (d) UD flax fabrics, (e) top and (f) side view of the 3D printed structure. The scale is the same for all pictures.
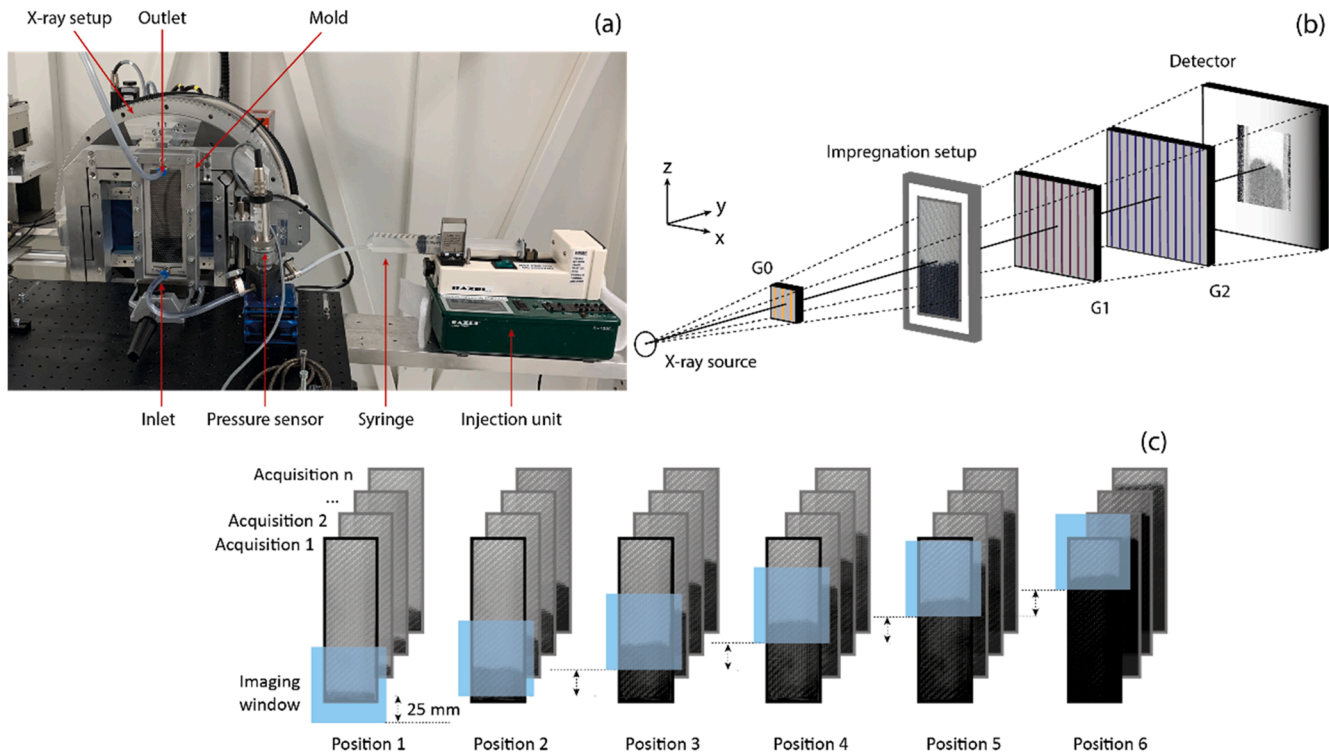

Fig. 2. (a) Impregnation setup, (b) schematic of the X-ray phase contrast imaging system and (c) illustration depicting the flow acquisition procedure.

2. Materials and methods

2.1. Materials

Five porous media were selected: four fibrous reinforcements whose properties are listed in Table 1 and a 3D printed structure. The twill glass fabric (Fig. 1a), previously utilized by Caglar et al. in [38,75] and the unidirectional carbon fabric (Fig. 1b) (with glass threads in the weft direction to maintain the position of the carbon tows), were used in this work as translucent and non-translucent fabrics respectively. Twill flax (Fig. 1c) and unidirectional flax (with a polymeric thread to maintain the structure) (Fig. 1d) fabrics were employed as alternative non-translucent preforms. The orientation of fabric reinforcements was 0° for all experiments. The 3D printed structure (Fig. 1e and f) was based on the geometry designed by Morren et al [76] and reproduced by a FlashForge Hunter Digital Light Processing (DLP) 3D printer with the resin FlashForge FH110. The structure was a grid of 3 mm thickness, with macro spaces interconnected with micro channels to mimic a textile-like solid.

The test fluid was an aqueous solution of poly(ethylene glycol) (PEG) (M_w = 35 kDa, Sigma Aldrich) at a concentration of 16.7 wt%. The density of this fluid is 1.026 g/ml, the viscosity at 20 °C 0.11 Pa.s and the surface tension 57.3 mN/m as previously characterized by Salvatori et al. [23]. These properties are similar to those of thermosetting resins typically used in composite manufacturing. For optical experiments with the glass fabric, around 0.08 wt% of Rhodamine B colorant from Carl Roth, which provides a strong coloration, was added to the fluid.

2.2. Flow experiments

Flow experiments were carried out with the setup shown in Fig. 2a. Porous structures were fitted in the cavity of a metal spacer with an inner silicon joint to minimize race tracking, then enclosed in between transparent top and bottom parts placed in between metal frames fastened with fourteen screws. Poly(methyl methacrylate) was used as transparent mold halves as it does not scatter X-rays; its thickness was optimized to reach a compromise between minimum noise in the X-ray images which results from absorption of the PMMA and maximum rigidity to minimize the deflection of the setup and was eventually set to 15 mm for each half. Metal spacers of different thicknesses were employed to vary the mold cavity thickness. Fabrics were cut to a width of 4.95 ± 0.05 cm and a length of 15 cm. The printed structure had a dimension of 5 cm × 12 cm, the length was limited by the maximal printing size of the 3D printer. Reinforcements were impregnated

Table 2
Impregnation experiments.

#	Fabric	Layers	Thickness [mm]	V_f [%]	Flow front velocity [mm/s]	Ca (10^{-3})
1	Twill Glass	9	3	45	0.13	0.25
2	Twill Glass	9	3	45	0.23	0.44
3	Twill Glass	9	3	45	0.48	0.92
4	UD Carbon	9	3	45	0.26	0.50
5	UD Carbon	9	2.5	54	0.22	0.42
6	UD Carbon	9	3.5	39	0.23	0.44
7	UD Carbon	6	2	45	0.25	0.48
8	UD Carbon	3	1	45	0.22	0.42
9	UD Carbon	12	4	45	0.27	0.52
10	UD Carbon	15	5	45	0.27	0.52
11	UD Carbon	18	6	45	0.27	0.52
12	Twill Flax	3	2	35	0.16	0.31
13	UD Flax	6	2	35	0.12	0.23
14	3D structure	1	3	–	0.15	0.28

vertically from bottom to top (z-direction) at constant flow rate thanks to an injection unit R-100E syringe pump from Razel Scientific Instruments. Contribution of the hydrostatic pressure buildup due to the vertical position, assumed to be maximum 1.5 kPa, was neglected as it was limited due to low density of the fluid and short impregnation length. A sensor, Keller Series 35XHTT, was placed close to the inlet in order to monitor the fluid pressure and temperature all along the impregnation.

The phase contrast X-ray imaging apparatus was a Talbot-Lau grating interferometer developed within the EVITA project [64]. The system allows imaging an area of approximatively 70 mm × 70 mm per acquisition and incorporates a moving platform to scan larger parts, whose movement can be synchronized with the image acquisition. The grating lines of the gratings G1 and G2 (Fig. 2b) are positioned along the z-direction and the grating movement is carried out in the x-direction. The following images are simultaneously provided at each measurement: absorption, refraction (associated respectively to the attenuation and refraction coefficients) and scattering, which is linked to the ultra-small angle X-ray scattering of the beam inside the sample, in turn related to a variation of the electronic density of the sample at the microscopic level [77]. Images present a resolution of 1334 × 1331 pixels and were taken from a series of 7 phase steps with an exposure time of 700 ms at each step, resulting in an averaged time of 9.2 s per acquisition. The additional time (9.2 s − 7x700 ms) is the duration required to transfer data between phase steps. The acceleration voltage of the X-ray tube was 60 kV. We performed preliminary tests to define

the required X-ray setup parameters and acquisition times in order to obtain scattering images with a satisfactory resolution and a good fluid/fabric contrast.

To track the impregnation along the reinforcement length, we developed an acquisition procedure with the X-ray system by synchronizing the stage movement and the flow speed (Fig. 2c). First, we defined six different positions corresponding to five vertical stage movements of 25 mm and we carefully centered the setup within the acquisition window in order to locate the flow front in the center of the resulting image. Then, we performed the following steps: (i) before launching the impregnation, a scanning of the dry reinforcement at one acquisition per position was carried out to construct a grey scale image of the dry state; (ii) for each impregnation experiment, the number of acquisitions per position was defined as a function of the flow speed (estimated by the measured averaged front velocity from preliminary optical experiments and using the set constant flow rate); (iii) once the fluid reached the outlet, the impregnation was continued at least 5 min and up to 15 min for slow flow conditions to ensure a complete saturation of the fabric and a third scan was performed at one acquisition per position to construct a grayscale image of the wetted fabric. Since the system calibration is sensitive to changes in ambient conditions, calibration was performed at the beginning dry, impregnation and wet acquisitions.

An overview of the experimental campaign is given in Table 2. Impregnation of the twill glass fabric (constant number of layers and volume fraction) was carried out at three flow rates. As the aim of this work is to demonstrate the potential of the method for non-translucent
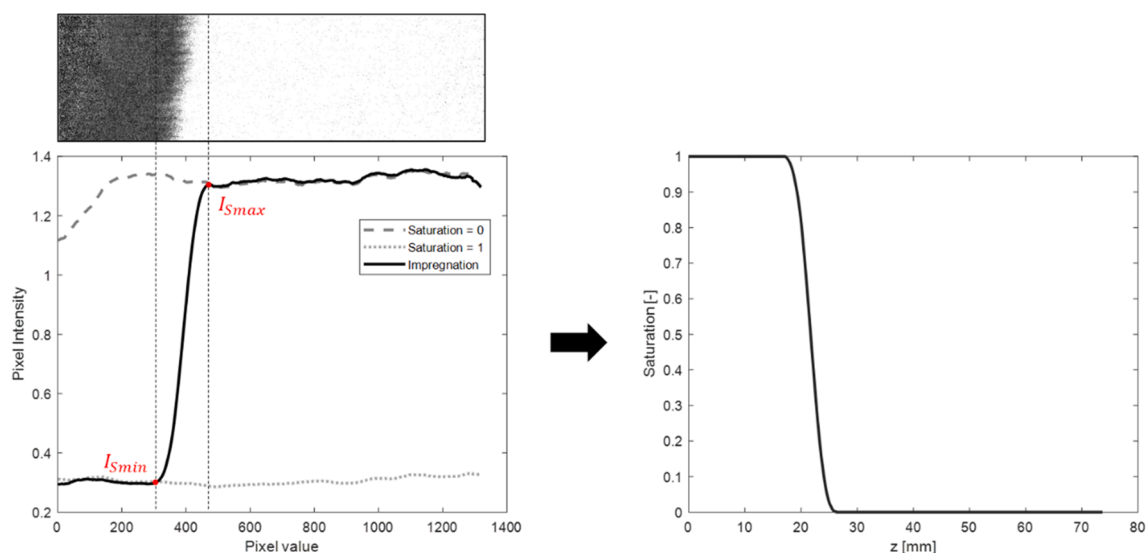

Fig. 3. Methodology for the construction of S(z) curve from the grayscale scattering image (example taken from an acquisition of test #4).
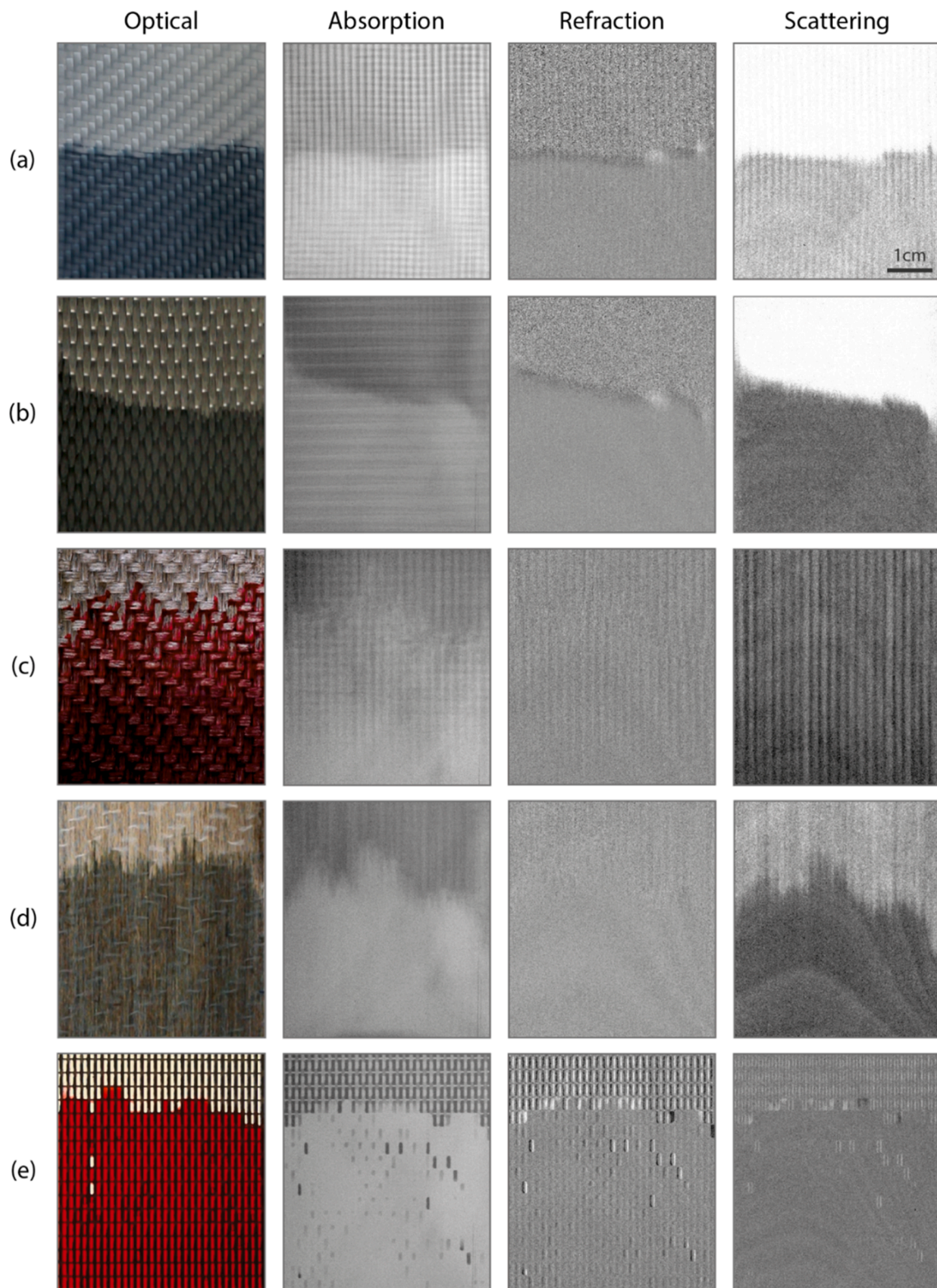
Fig. 4. Example of flow patterns observed in optical, absorption, refraction and scattering images obtained for the different reinforcements (a) Twill Glass (test #2), (b) UD Carbon (test #4), (c) Twill Flax (test #12), (d) UD Flax (test #13) fabrics and (e) the 3D printed structure (test #14). The image of the optical view does not correspond to the flow shown in X-ray images as the X-ray infrastructure did not allow capturing videos during X-ray measurements. The scale is the same for all pictures.

fabrics, different tests were carried out with the carbon fabric, in particular to analyze the effect of the number of layers and the volume fraction on scattering images' contrast. Finally, one experiment was performed for each of the following porous media: the two flax fabrics

(twill and UD) with the same volume fraction and the 3D printed structure.

Flow experiments with the translucent glass reinforcement were conducted under X-ray phase contrast imaging and repeated in the
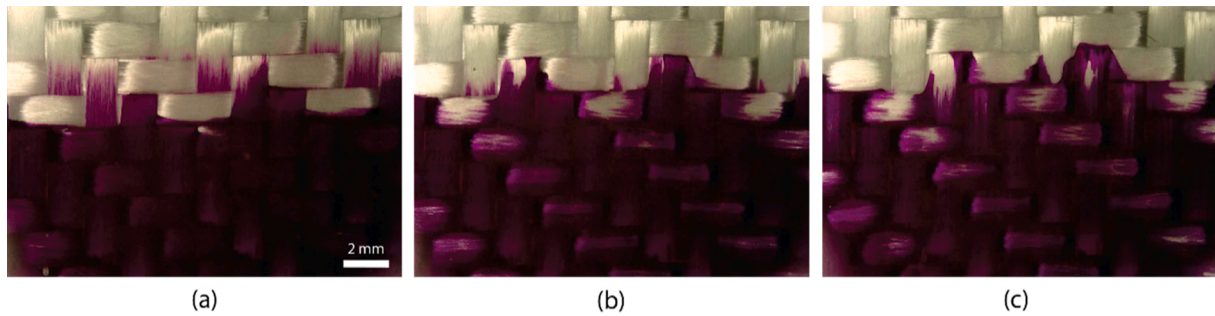
Fig. 5. Flow patterns imaged by a digital microscope (a) test #1 (b) test #2 (c) test #3. The scale is the same for all pictures.

laboratory under conventional optical methods to provide a validation of the proposed visualization method. The advancement of the flow was thus recorded through the transparent mold by a digital camera Canon EOS700D; the video acquisition was set to 30 frames per second with a resolution of 1920 × 1080 pixels. The corresponding dynamic saturation curves were built adapting the methodology of Nordlund et al. [9] and were thereafter compared with the curves obtained by X-ray image analysis.

2.3. Image analysis

The progressive saturation of the preforms was obtained from scattering images. Prior to the analysis of the grayscale intensities, we applied an image processing routine to each set of images corresponding to a given experiment. Images were rotated to correct the verticality, cropped by selecting a study area with a width of 400 pixels (roughly corresponding to a width of 2.2 cm) to get rid of flow edge effects and smoothed with a mean average filter. To assess the saturation versus the position curve $S(z)$ from the scattering image, we used a methodology based on defining the deviation of the grayscale values of the images acquired during the impregnation from that of images acquired at completely dry and wet states as also illustrated in Fig. 3. The light area of the scattering image corresponds to the fabric and the dark one to the fluid, since it is homogeneous and does not scatter X-rays. In the frame of this work, we assumed that the pixel intensity of the wetted fabric scans corresponds to a saturation equal to 1 and do not take into account the presence of possible small pores remaining after full impregnation. For all images, the averaged pixel intensity value over each column was calculated, i.e., average along the part width was calculated. Then, for each position, we generated the pixel intensity versus pixel position curves of the dry and wetted fabric and compared them to the impregnation curves of that position. Three zones were thereafter distinguished: fully saturated, unsaturated area and dry fabric. The pixel intensity value I_{Smin} defines the transition between the fully and partially saturated zones and I_{Smax} the transition between the unsaturated zone and the dry fabric. Finally, we converted each pixel intensity value into a saturation value by linear interpolation. The position z in pixels was converted into millimeters by using a pixel size of 54 μm. Since all the instances linked to the image acquisition are recorded by the X-ray system and the displacement of the stage is known, it is possible for each experiment to build the $S(z)$ curve for all acquisitions in a single graph. Moreover, all the obtained curves during an experiment can be unified by plotting the dynamic saturation $S(z,t)$ curve as Nordlund et al. [9] suggested for constant flow rate experiments.

3. Results

3.1. Validation

Absorption, refraction and scattering images obtained for the glass fabric impregnation (test #2) by X-ray phase contrast are presented in Fig. 4a. A good contrast between the fabric and the fluid is revealed by
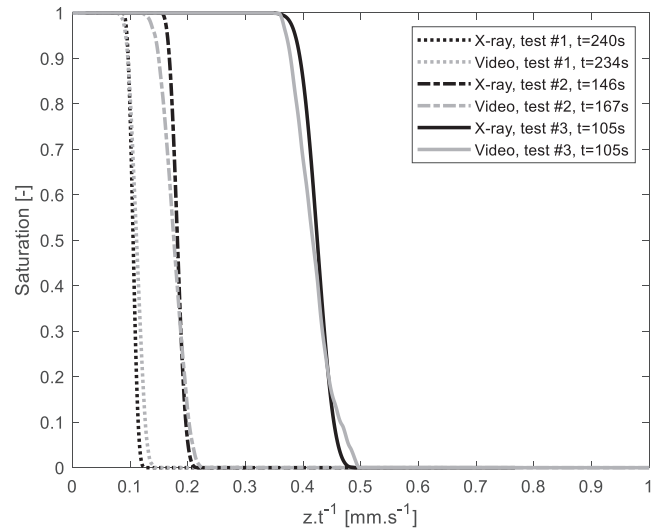

Fig. 6. Comparison of S(z,t) curves built from optical and X-ray acquisitions.

the scattering image, whereas the absorption and refraction images exhibit very low contrast, with a barely visible flow front. The absorption image highlights the fabric structure which can be assimilated to a square grid. Compared to absorption images, in scattering and refraction images, the fabric structure was only identified in the vertical direction because of the grating configuration in the X-ray setup [78]. The dry and wet areas of the fabric can be differentiated in the refraction image since the structural pattern disappears when the fabric is fully saturated.

We visualized the flow front patterns of the three glass fabric impregnations by performing them under a Keyence digital microscope. The resulting images displayed in Fig. 5 revealed that the unsaturated zone increases with flow speed. At the low capillary number, $Ca = 2.5 \cdot 10^{-4}$, test #1 (Fig. 5a), we observe a narrow unsaturated zone, corresponding to balanced capillary and viscous forces, nonetheless capillary driven fluid flow is observed in the tows. For the medium capillary number $Ca = 4.4 \cdot 10^{-4}$, test #2 (Fig. 5b), the fluid first fills the inter-tow spaces; the tows behind the flow front are not completely saturated thus indicated a viscous flow. The fastest flow with a higher capillary number $Ca = 9.2 \cdot 10^{-4}$, test #3 (Fig. 5c), presented the same trend as observed in Fig. 5b but with a large unsaturated zone and had

Table 3
Comparison of flow progression during in-operando flow imaging.

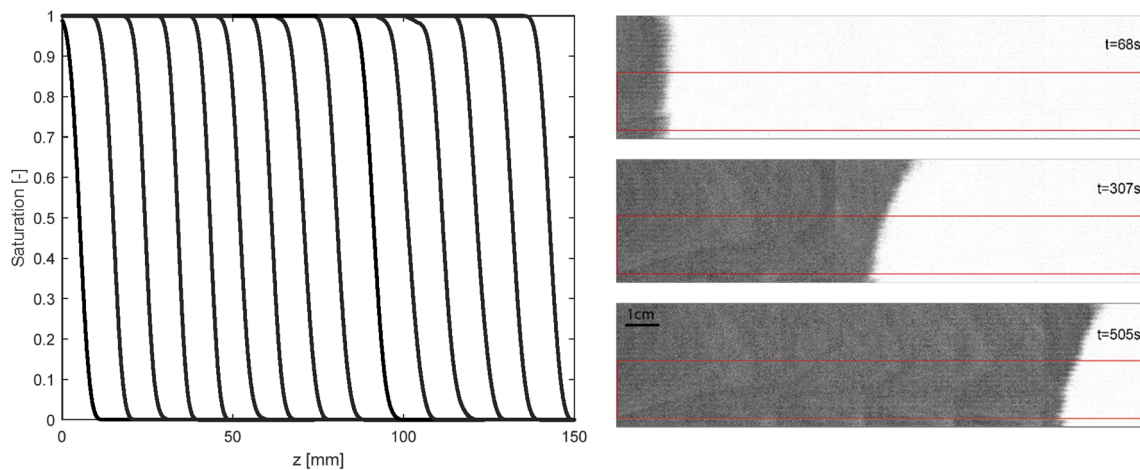| Acquisition method	Image acquisition time [s]	Flow displacement per image acquisition [mm]		
		test #1	test #2	test #3
X-ray	9.2	1.20	2.12	4.42
Video	0.04	0.005	0.01	0.02

Fig. 7. S(z) curves for the impregnation of test #4 taken every 4 acquisitions (right). A reconstruction of the impregnation along the fabric length for three different times with the measurement zone is highlighted in red (left).

thus a more viscous behavior.

We constructed the dynamic saturation curves $S(z,t)$ of tests #1, #2 and #3 by optical and X-ray image methods. Fig. 6 compares the resulting curves and reveals a clear agreement between the two methods. Nevertheless, some deviations were noticed; in particular, the unsaturated area is slightly larger for all curves derived from the optical acquisition (i.e., the curves from x-ray radiography are steeper). We attributed this difference to the fact that the flow is observed only from the surface in the video acquisition where wall effects take place [79] whereas the flow is thickness averaged in X-ray acquisition. In addition, we calculated flow displacements of the three tests during one single image acquisition for both imaging methods (Table 3). It should be

noted that a phase-dependent anticipation or delay of the flow was observed during fast impregnations resulting in a lower precision on the saturation measurement. This effect could be minimized in improved set-ups by reducing the acquisition time with a more powerful X-ray source and/or optimizing the grating geometry which was initially developed for static measurements. Considering the curve shapes, the steeper curve with the narrower unsaturated zone corresponds to the more balanced flow (test #1), while with increasing flow speed, the saturation curves become less steep (test #2 and test #3). These observations are in good agreement with the observations from Fig. 5, and correlate with the results found by Nordlund et al. [9] establishing the direct link between the shape of the saturation curve and the flow rate,
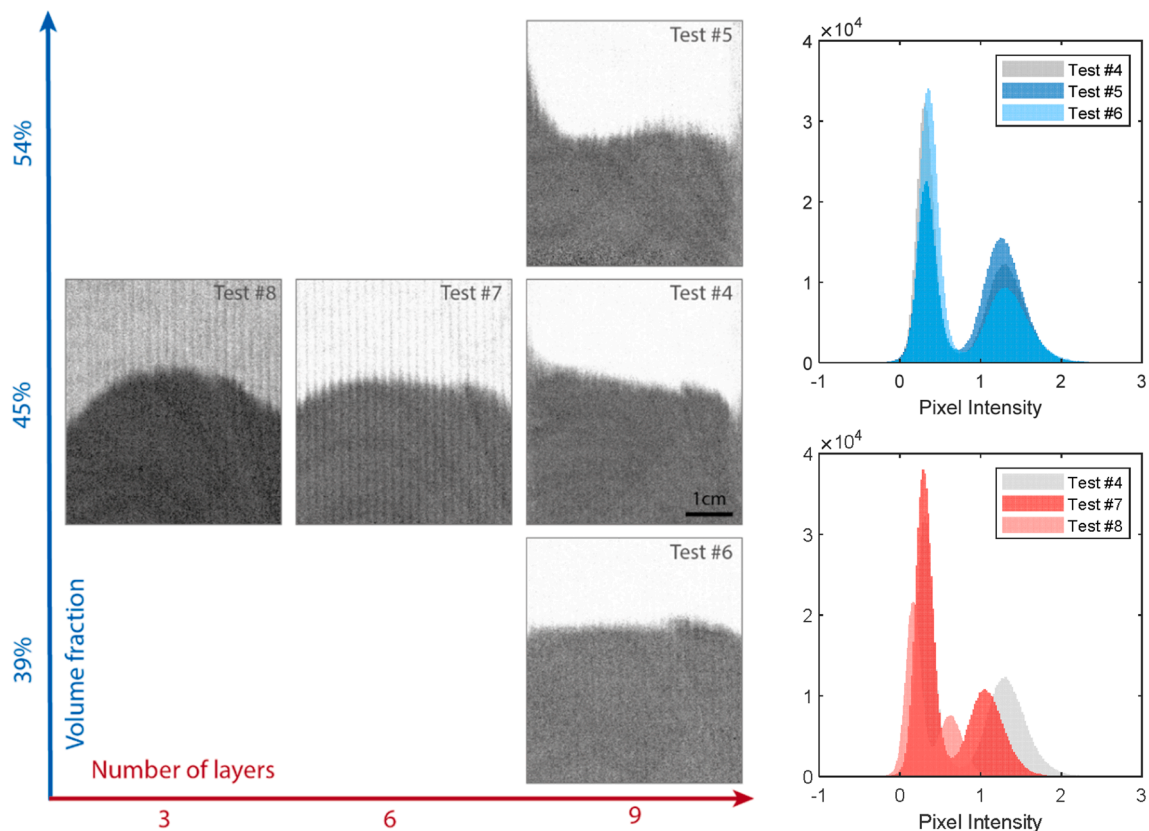

Fig. 8. Comparison of scattering images obtained for the different impregnation configurations of the carbon fabric with the corresponding histograms. The scale is the same for all pictures.
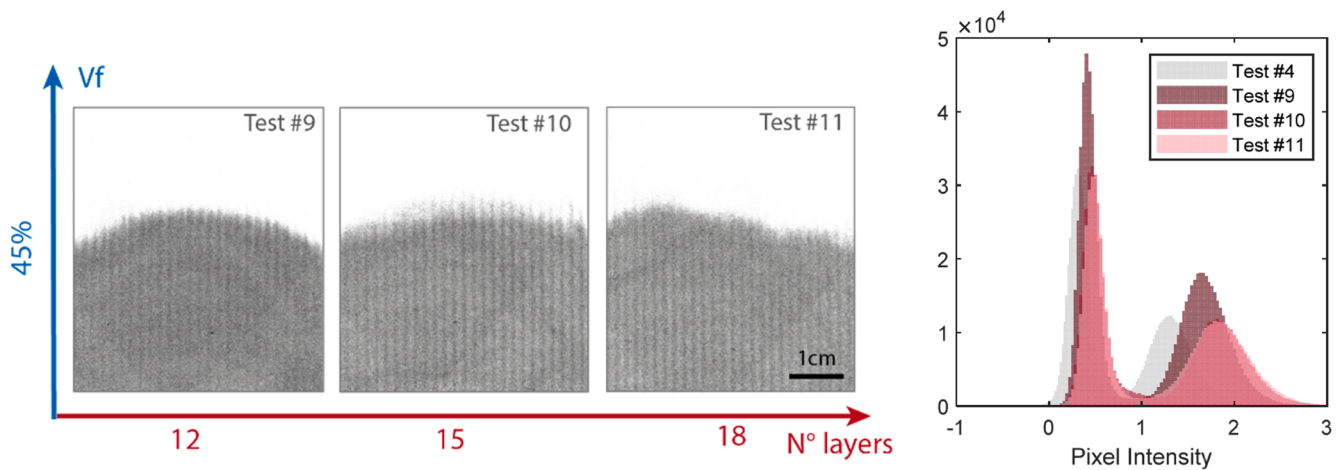
Fig. 9. Comparison of scattering images obtained for tests #9, #10 and #11 with the corresponding histograms which are compared to the one of test #4. The scale is the same for all pictures.

because the wetting conditions are dynamic.

3.2. Carbon fabric

Our approach allows capturing the thickness averaged flow front location during impregnation of non-translucent carbon fabrics with acquisition times below 10 s, transcending previously reported approaches. Once we validated our method, we sought to visualize fluid flow through non-translucent preforms, in particular carbon fabrics. Test #4 was defined as a reference sample and its corresponding absorption, refraction and scattering images are displayed in Fig. 4b. Interestingly, the scattering image for carbon fabric revealed a better fluid-fabric contrast as compared to glass fabric. As expected, the carbon fabric did not show much contrast in absorption images, however the glass stitches clearly appeared. In the scattering images, the glass stitches were also identified by the pixel intensity, which was slightly lower in the zones where the glass stitches were present compared to areas with only carbon. This observation proves the convenience of the proposed technique for the study of flow through preforms made up of different materials. Finally, as for the glass fabric, no significant contrast was obtained from the refraction image. Spaces between the tows are visible in scattering and refraction images in the form of vertical lines, albeit thinner compared to those of the glass fabric as the structure is more compact.

For all impregnations carried out with the carbon fabric, we built the saturation curve $S(z)$ for each acquisition. Fig. 7 shows the constructed saturation curves for a subset of collected images during the test #4 and the reconstructed impregnations along the fabric length for three different times. Successive curves in the figure are separated by approximately 37 s. Based on the graph, the saturation decreases almost linearly over the unsaturated region. For all curves, the slope is nearly identical as expected since the fluid was injected at a constant flow rate and the impregnation conditions were invariable along the fabric length and time.

We investigated the role of fiber volume fraction (by compressing a pre-determined number of layers to different thicknesses) and the role of the number of layers (by compressing several numbers of layers leading to the same fiber volume fraction at different thicknesses). Fig. 8 shows that the contrast increases (as well as the signal-to-noise ratio) in the scattering images with the number of layers. According to literature, the scattering signal increases with the porosity level as well as the pore size [64,80–82]. Considering that transitions between air and material act as the X-ray scattering inhomogenities and that the number of scattering events thus increase as the number of layer increases, our observations are aligned with the underlying physical phenomena. On the other hand,

the change in number of scattering transitions due to change in volume fraction (while having same number of fabric layers) is limited since the same number of fibers are present in the cavity and this is why, experiments #4, 5 and 6 resulted in similar scattering images. Therefore, the main scattering arises from the fiber-pore transitions. The change in the size of pores created between the fibers is not significant enough to contribute to the scattering signal.

With the aim of further investigating the effect of the number of layers on the pixel intensity, we performed three additional tests in which we increased the number of layers to 12, 15 and 18. From the scattering images Fig. 9, we do not observe an apparent change in the contrast between the two phases (fluid and fabric). In the histograms (Figs. 8 and 9), the low value peak corresponds to the dark area (wetted fabric), the high value peak to the white area (dry fabric) and the contrast is defined by the separation of these two peaks. Increasing the number of layers results in a greater separation between the two peaks and thus more contrast. However, between 15 and 18 layers, histograms are almost superposed and contrast cannot be further enhanced by increasing the number of layers.

3.3. Flax fabrics

Fig. 4c and Fig. 4d show, respectively, the images obtained for tests #12 with the twill and #13 with the unidirectional flax fabrics. In the scattering images, the flow front is barely visible for test #12 whereas it is clearly observed in test #13. Based on our previous results with carbon fabric, this difference in contrast is related to the number of layers used. For both samples, the absorption image brought the flow pattern out which was directly linked to the fabric structure. In the weave case, the unsaturated zone is larger because large pores created by the weft and warp tows enhance viscous flow between tows while intra-tow spaces require longer time scales for impregnation. Conversely, the unidirectional fabric presents a more compact structure with more evenly distributed pores in which the fluid cannot easily progress in between the tows and the boundary is crisper. Notwithstanding the reduced contrast obtained for flax fabrics compared to carbon and glass fabrics, the present results provide a stimulus for further investigation of flow through natural preforms with X-ray phase contrast imaging. With the aim of enhancing the contrast, we performed additional tests after increasing the number of layers to 12 and 9 for the UD and Twill flax fabrics respectively. The contrast slightly improved but was far from reaching a level comparable to that observed in glass or carbon fabrics. In order to better visualize impregnation of natural fiber preforms with the present technique, other solutions can be explored such as changing the fluid nature or increasing the X-ray source power.
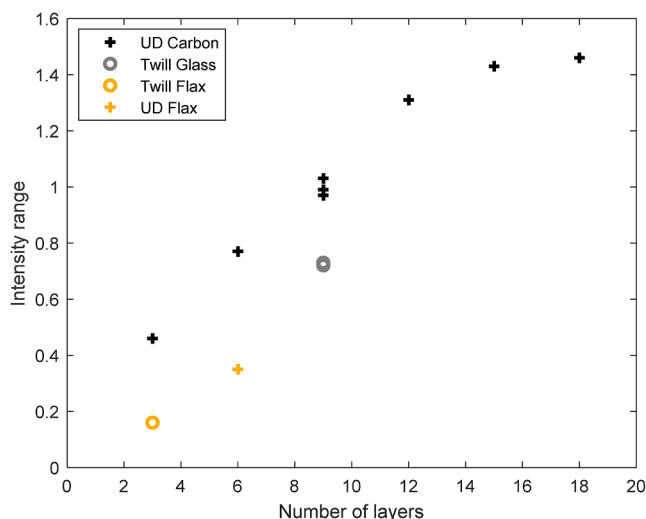
Fig. 10. Intensity range of scattering images versus the fabric number of layers.

Table 4

Absorption and refraction properties of carbon, silica and cellulose at 60 keV from [85,86].

Material	Formula	μ [m^{-1}]	δ (10^{-7})
Water	H$_2$O	0.21	0.6
Carbon	C	0.32	2.0
Glass	SiO$_2$	0.63	1.5
Flax	C$_{12}$H$_{10}$O$_5$	0.24	0.8

3.4. Polymeric structure

The obtained images corresponding to the polymeric structure impregnation (test #14) are shown in Fig. 4e. No significant contrast was obtained for the scattering image between the grid and the fluid since the grid is a homogeneous material and the porosities are in the range of a millimeter. In addition, the fluid path in between the small pores of the structure was hidden by the polymeric structure. Vertical lines corresponding to the edges of the large cavities were the only elements that were barely visible. Absorption images revealed more interesting results: the location of the small cavities was clearly distinguished, corresponding to less dense zones where the grid appeared lighter, the fluid path was easily tracked and empty, partially-filled and filled cells were clearly highlighted. Thus, the observation of flow through 3D printed polymeric porous preforms under X-ray techniques is enhanced by attenuation rather than scattering and this approach could be extended to more complex networks for fluid dynamics studies. This example shows at the same time the limitation and versatility of the presented technique.

4. Discussion

In order to quantitatively compare the contrast obtained in scattering images for the studied fibrous reinforcements, we defined an intensity range value for each sample by the subtraction of I_{Smin} from I_{Smax}. The obtained values for all the samples versus the number of layers are plotted in Fig. 10. The three main factors responsible for the contrast are presented below.

4.1. Effect of the number of layers and fiber diameter

As we pointed out in previous sections, the volume fraction has a minimal effect on the scattering contrast; however, the contrast strongly depends on the number of layers since the fibers act as main scatterers. This observation is highlighted in Fig. 10, in particular for the unidirectional carbon fabric: a linearity is observed between the signal intensity and the number of layers till it reaches a saturation value. As previously pointed out, fiber-pore transitions act as main scatters and highly influence the signal. Fibers with larger diameters have lower specific surface area per volume compared to fibers with smaller diameters and thus will create fewer scattering events. Indeed, fibers with a diameter comparable to the grating size (4 µm), are in the "sensitive size window" [77] and scatter the X-ray signal better, resulting in an enhanced contrast. As presented in Table 1, fiber diameters are in line

with the obtained contrast. Glass and carbon fabrics which have fibers with diameters of less than 10 µm gave better contrast compared to flax fabrics which possess fibers with significantly larger diameters. As carbon and glass fabrics have similar diameters, the contrast difference between them in the scattering images arises mostly from their refraction coefficients.

4.2. Effect of the material composition

The highest contrast between the reinforcement and the fluid was achieved with carbon fabric, thereupon glass and finally flax (Fig. 10). According to the literature, inhomogeneities that create scattering refer to variations in the electron density which are related to the materials' refraction coefficient δ [83]. In Table 4, linear absorption coefficient μ and refraction coefficient δ from tabulated databases are presented for the different materials at the X-ray intensity used in the present work, assuming that water is the main element of the fluid mixture, carbon that of carbon fibers, silica and cellulose those of the glass and flax fibers respectively. Refraction coefficients prove to be directly linked to the scattering ability of each material. Concerning the refraction images, the flow front was pinpointed for glass and carbon samples because their refraction coefficients are high enough compared to those of the fluid (even though no significant difference was observed between them since the values are in the same range). However, for flax fabrics, the front was hardly detected given the proximity of the cellulose and fluid refraction coefficients. The absorption coefficient is directly linked to the density and this is why glass showed higher contrast in the absorption image.

4.3. Effect of the structure

The fabric configuration influences the scattering contrast. For a given material, more compact and homogeneous fabric layers with fibers parallel to the grating lines provide a higher contrast. In the present work, we visualized unidirectional and twill fabrics. In the case of unidirectional configuration where the fibers were parallel to the grating lines, we obtained a stronger signal with respect to the twill configuration. In refraction and scattering images, variations on the x-direction (perpendicular to the grating lines) are only measured and thus variations on the z-direction such as the horizontal bundles of the twill fabrics do not appear on those images. By rotating the fabric and thus creating an angle between the gratings and vertical/horizontal bundles, it would be possible to observe weft and warp directions of twill fabrics. We repeated test #4 by rotating the setup around the y-axis by 45° (test #15) for a glimpse of the influence of the fabric orientation: an example of scattering image is shown in Fig. 11. As expected, the fabric weave patterns are observed in x and z directions while the contrast is decreased at 45°.

4.4. Dual scale flow patterns

Finally, we sought to explore the potential of X-ray phase contrast imaging to observe dual scale flow patterns [84] by combining absorption and scattering images analogously to what was done by Senck et al. [67] for dual scale characterization of cracks in fiber reinforced composites. The idea is to create a superimposed image by using the power of each technique as the dark field image is sensitive to subpixel
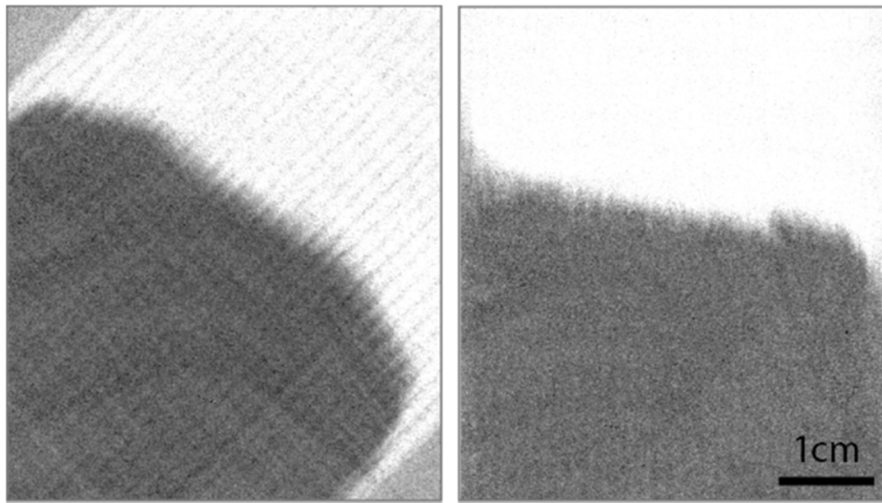
Fig. 11. Scattering image resulting of rotating the setup 45° (test #15) compared to the scattering image of test #4.
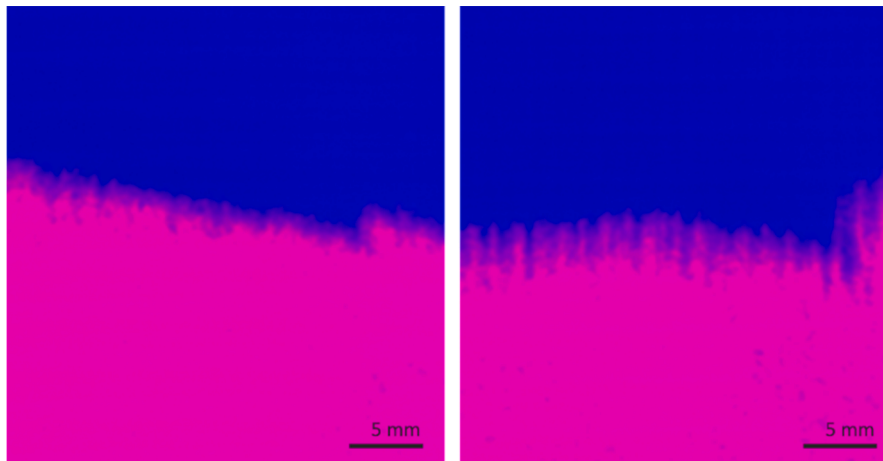

Fig. 12. Superimposed absorption and scattering images for visualization of flow patterns. Acquisition corresponding to test #4 (left) and test #16 (right).

variations and thus the fabric porosity, while the absorption image depends on the material density and elucidates the fabric macrostructure. For that, we compare test #4 to an additional impregnation (test #16) performed with the same conditions but increasing the flow rate, leading to a flow front speed of 0,58 mm/s corresponding to a capillary number $Ca = 1.11 \cdot 10^{-3}$. For both experiments, we applied a Gaussian filter to the resulting images, then used the Red-Green-Blue (RGB) coding, by attributing the B and R channels to absorption and scattering images respectively to construct the superimposed images shown in Fig. 12. Promising results were obtained: fingering between the tows is clearly identified for test #16 as compared to test #4, indicating a viscous flow dominated pattern with a larger unsaturated zone.

5. Conclusions

X-ray phase contrast imaging is proved to be a powerful tool to visualize in-operando the dynamic fluid flow across the thickness of translucent and non-translucent fibrous preforms. In particular, we observed the progressive saturation of carbon fabric preforms by collecting images with an acquisition time of less than 10 s, and on a relatively large sample size window of 7 cm x 7 cm. A methodology to build the saturation curve by analyzing the grayscale of dark field images was presented. Taking advantage of the wide range of materials that this technique can visualize, glass preforms were used for validating

the current method by comparing the resulting progressive saturation through glass preforms by X-ray and conventional optical techniques. The visualization method was then extended to carbon and flax fabrics and a 3D printed preform. By comparing different geometric and flow velocity configurations, we identified the main parameters affecting the scattering contrast, including the number of layers, the fiber diameter, the refraction properties of the material as well as the fabric structure. This provides guidelines for the in-depth analysis of flow patterns, in particular in non-transparent carbon fabrics, with model fluids or reactive resins, for model validation and identification of the relevant parameters governing flow in liquid composite molding processes.

Declaration of Competing Interest

The authors declare that they have no known competing financial

interests or personal relationships that could have appeared to influence the work reported in this paper.

Acknowledgements

This work was supported by the Swiss National Science Foundation (SNF n° 200021_182669). The authors sincerely acknowledge Jeroen Staal for his contribution during the experimental work and Thomas Stadelmann and Guido Spinola for their support with the X-ray phase contrast imaging. Bcomp™ (Fribourg, Switzerland) is thankfully acknowledged for having provided the flax fabrics.

References

[1] Ruiz E, Achim V, Soukane S, Trochu F, Bréard J. Optimization of injection flow rate to minimize micro/macro-voids formation in resin transfer molded composites. Compos Sci Technol 2006;66:475–86. https://doi.org/10.1016/j.compscitech.2005.06.013.

[2] Gourichon B, Binetruy C, Krawczak P. Experimental investigation of high fiber tow count fabric unsaturation during RTM. Compos Sci Technol 2006;66:976–82. https://doi.org/10.1016/j.compscitech.2005.07.032.

[3] Imbert M, Comas-Cardona S, Abisset-Chavanne E, Prono D. Experimental investigation of intra-tow fluid storage mechanisms in dual-scale fiber reinforcements. Compos Part A 2018;107:70–82. https://doi.org/10.1016/j.compositesa.2017.12.015.

[4] Bodaghi M, Lomov SV, Simacek P, Correia NC, Advani SG. On the variability of permeability induced by reinforcement distortions and dual scale flow in liquid composite moulding : A review. Compos Part A 2019;120:188–210. https://doi.org/10.1016/j.compositesa.2019.03.004.

[5] Mehdikhani M, Gorbatikh L, Verpoest I, Lomov SV. Voids in fiber-reinforced polymer composites : A review on their formation, characteristics, and effects on mechanical performance. J Compos Mater 2018. https://doi.org/10.1177/0021998318772152.

[6] Schell JSU, Deleglise M, Binetruy C, Krawczak P, Ermanni P. Numerical prediction and experimental characterisation of meso-scale-voids in liquid composite moulding 2007;38:2460–70. https://doi.org/10.1016/j.compositesa.2007.08.005.

[7] Yashiro S, Nakashima D, Oya Y, Okabe T, Matsuzaki R. Particle simulation of dual-scale flow in resin transfer molding for process analysis. Compos Part A 2019;121:283–8. https://doi.org/10.1016/j.compositesa.2019.03.038.

[8] Leclerc JS, Ruiz E. Porosity reduction using optimized flow velocity in Resin Transfer Molding. Compos Part A 2008;39:1859–68. https://doi.org/10.1016/j.compositesa.2008.09.008.

[9] Nordlund M, Michaud V. Dynamic saturation curve measurement for resin flow in glass fibre reinforcement. Compos Part A 2012;43:333–43. https://doi.org/10.1016/j.compositesa.2011.12.001.

[10] Park CH, Lebel A, Saouab A, Bréard J, Il W. Modeling and simulation of voids and saturation in liquid composite molding processes. Compos Part A 2011;42:658–68. https://doi.org/10.1016/j.compositesa.2011.02.005.

[11] Pillai KM. Modeling the Unsaturated Flow in Liquid Composite Molding Processes : A review and Some Thoughts. J Compos Mater 2004;38:2097–118. https://doi.org/10.1177/0021998304045585.

[12] Wolfrath J, Michaud V, Modaressi A. Unsaturated flow in compressible fibre preforms. Compos Part A Appl Sci Manuf 2006;37:881–9. https://doi.org/10.1016/j.compositesa.2005.01.008.

[13] Facciotto S, Simacek P, Advani SG, Middendorf P. Modeling of anisotropic dual scale flow in RTM using the finite elements method. Compos Part B 2021;214. https://doi.org/10.1016/j.compositesb.2021.108735.

[14] Zingraff L, Michaud V, Bourban PE, Månson JAE. Resin transfer moulding of anionically polymerised polyamide 12. Compos Part A Appl Sci Manuf 2005;36:1675–86. https://doi.org/10.1016/j.compositesa.2005.03.023.

[15] Park CH. Lee W Il. Modeling void formation and unsaturated flow in liquid composite molding processes : a survey and review 2011. https://doi.org/10.1177/0731684411411338.

[16] LeBel F, Ruiz E, Trochu F. Void Content Analysis and Processing Issues to Minimize Defects in Liquid Composite Molding. Polym Compos 2019;40:109–20. https://doi.org/10.1002/pc.24609.

[17] Michaud V. A Review of Non-saturated Resin Flow in Liquid Composite Moulding processes. Transp Porous Media 2016. https://doi.org/10.1007/s11242-016-0629-7.

[18] Gascón L, García JA, Lebel F, Ruiz E, Trochu F. A two-phase flow model to simulate mold filling and saturation in Resin Transfer Molding. Int J Mater Form 2016;9:229–39. https://doi.org/10.1007/s12289-015-1225-z.

[19] Gascón L, García JA, Lebel F, Ruiz E, Trochu F. Numerical prediction of saturation in dual scale fibrous reinforcements during Liquid Composite Molding. Compos Part A 2015;77:275–84. https://doi.org/10.1016/j.compositesa.2015.05.019.

[20] Léger A, Molina-Jordá JM, Weber L, Mortensen A. Percolation and Universal Scaling in Composite Infiltration Processing. Mater Res Lett 2015;3:7–15. https://doi.org/10.1080/21663831.2014.948692.

[21] Michaud V, Mortensen A. Infiltration processing of fibre reinforced composites : governing phenomena. Compos Part A Appl Sci Manuf 2001;32:981–96. https://doi.org/10.1016/S1359-835X(01)00015-X.

[22] Verrey J, Michaud V, Manson JA. Dynamic capillary effects in liquid composite moulding with non-crimp fabrics. Compos Part A Appl Sci Manuf 2006;37:92–102. https://doi.org/10.1016/j.compositesa.2005.04.011.

[23] Salvatori D, Caglar B, Teixidó H, Michaud V. Permeability and capillary effects in a channel-wise non-crimp fabric. Compos Part A 2018;108:41–52. https://doi.org/10.1016/j.compositesa.2018.02.015.

[24] Bréard J, Henzel Y, Trochu F, Gauvin R. Analysis of dynamic flows through porous media. Part I: Comparison between saturated and unsaturated flows in fibrous reinforcements. Polym Compos 2003;24(3):391–408. https://doi.org/10.1002/pc.10038. ISSN: 0272-8397, 1548-0569.

[25] Michaud V, Compton LM, Mortensen A. Capillarity in Isothermal Infiltration of Alumina Fiber Preforms with Aluminum. Metall Mater Trans 1994;25:2145–52. https://doi.org/10.1007/BF02652315.

[26] De Parseval Y, Pillai KM, Advani SG. A Simple Model for the Variation of Permeability due to Partial Saturation in Dual Scale Porous Media. Transp Porous Media 1997;27:243–64. https://doi.org/10.1023/A:1006544107324.

[27] Slade J, Pillai KM, Advani SG. Investigation of Unsaturated Flow in Woven, Braided and Stitched Fiber Mats During Mold-Filling in Resin Transfer Molding. Polym Compos 2001;22:491–505. https://doi.org/10.1002/pc.10554.

[28] Tan H, Roy T, Pillai KM. Variations in unsaturated flow with flow direction in resin transfer molding : An experimental investigation. Compos Part A Appl Sci Manuf 2007;38:1872–92. https://doi.org/10.1016/j.compositesa.2007.04.002.

[29] Bayldon JM, Daniel IM. Flow modeling of the VARTM process including progressive saturation effects. Compos Part A 2009;40:1044–52. https://doi.org/10.1016/j.compositesa.2009.04.008.

[30] Matsuzaki R, Seto D, Todoroki A, Mizutani Y. Void formation in geometry – anisotropic woven fabrics in resin transfer molding. Adv Compos Mater 2014;23:99–114. https://doi.org/10.1080/09243046.2013.832829.

[31] Matsuzaki R, Seto D, Todoroki A, Mizutani Y. In situ void content measurements during resin transfer molding. Adv Compos Mater 2013;22:239–54. https://doi.org/10.1080/09243046.2013.801822.

[32] Causse P, Ravey C, Trochu F. Capillary Characterization of Fibrous Reinforcement and Optimization of Injection Strategy in Resin Transfer Molding. J Compos Sci 2018;2. https://doi.org/10.3390/jcs2020019.

[33] Lebel F, Fanaei AE, Ruiz E. Prediction of optimal flow front velocity to minimize void formation in dual scale fibrous reinforcements. Int J Mater Form 2014:93–116. https://doi.org/10.1007/s12289-012-1111-x.

[34] Lebel F, Fanaei AE, Ruiz É, Trochu F. Experimental Characterization by Fluorescence of Capillary Flows in the Fiber Tows of Engineering Fabrics. Open J Inorg Non-Metallic Mater 2012;2:25–45. https://doi.org/10.1177/0040517512471742.

[35] Lebel F, Ruiz E, Trochu F. Experimental study of saturation by visible light transmission in dual-scale fibrous reinforcements during composite manufacturing. Reinf Plast Compos 2017;36:1693–711. https://doi.org/10.1177/0731684417725187.

[36] Chen B, Chou T. Compaction of woven-fabric preforms: nesting and multi-layer deformation. Compos Sci Technol 2000;60:2223–31. https://doi.org/10.1016/S0266-3538(00)00017-8.

[37] Yousaf Z, Potluri P, Withers PJ. Influence of Tow Architecture on Compaction and Nesting in Textile Preforms. Appl Compos Mater 2017;24:337–50. https://doi.org/10.1007/s10443-016-9554-8.

[38] Caglar B, Tekin C, Karasu F, Michaud V. Assessment of capillary phenomena in liquid composite molding. Compos Part A 2019;120:73–83. https://doi.org/10.1016/j.compositesa.2019.02.018.

[39] Villière M, Guéroult S, Sobotka V, Boyard N, Bréard J. Dynamic saturation curve measurement in liquid composite molding by heat transfer analysis. Compos Part A 2015;69:255–65. https://doi.org/10.1016/j.compositesa.2014.11.024.

[40] Gueroult S, Lebel-Lavacry A, Park CH, Bizet L, Saouab A, Bréard J. Analytical modeling and in situ measurement of void formation in liquid composite molding processes. Adv Compos Mater 2014;23:31–42. https://doi.org/10.1080/09243046.2013.862383.

[41] Carlone P, Palazzo GS. Unsaturated and Saturated Flow Front Tracking in Liquid Composite Molding Processes using Dielectric Sensors. Appl Compos Mater 2015;22:543–57. https://doi.org/10.1007/s10443-014-9422-3.

[42] Carlone P, Rubino F, Paradiso V, Tucci F. Multi-scale modeling and online monitoring of resin flow through dual-scale textiles in liquid composite molding processes. Int J Adv Manuf Technol 2018;96:2215–30. https://doi.org/10.1007/s00170-018-1703-9.

[43] Endruweit A, Glover P, Head K, Long AC. Mapping of the fluid distribution in impregnated reinforcement textiles using Magnetic Resonance Imaging : Application and discussion. Compos Part A 2011;42:1369–79. https://doi.org/10.1016/j.compositesa.2011.05.020.

[44] Endruweit A, Glover P, Head K, Long AC. Mapping of the fluid distribution in impregnated reinforcement textiles using Magnetic Resonance Imaging : Methods and issues. Compos Part A 2011;42:265–73. https://doi.org/10.1016/j.compositesa.2010.11.012.

[45] Ravey C, Ruiz E, Trochu F. Determination of the optimal impregnation velocity in Resin Transfer Molding by capillary rise experiments and infrared thermography. Compos Sci Technol 2014;99:96–102. https://doi.org/10.1016/j.compscitech.2014.05.019.

[46] Lystrup C, George A, Zobell B, Boster K, Childs C, Girod H. Optical measurement of voids in situ during infusion of carbon reinforcements. J Compos Mater 2020. https://doi.org/10.1177/0021998320959820.

[47] Vilà J, Sket F, Wilde F, Requena G, González C, Llorca J. An in situ investigation of microscopic infusion and void transport during vacuum-assisted infiltration by

means of X-ray computed tomography. Compos Sci Technol 2015;119:12–9. https://doi.org/10.1016/j.compscitech.2015.09.016.

[48] Bhattad P, Willson CS, Thompson KE. Effect of Network Structure on Characterization and Flow Modeling Using X-ray Micro-Tomography Images of Granular and Fibrous Porous Media. Transp Porous Med 2011;90:363–91. https://doi.org/10.1007/s11242-011-9789-7.

[49] Larson NM, Zok FW. Insights from in-situ X-ray computed tomography during axial impregnation of unidirectional fiber beds. Compos Part A 2018;107:124–34. https://doi.org/10.1016/j.compositesa.2017.12.024.

[50] Larson NM, Cuellar C, Zok FW. X-ray computed tomography of microstructure evolution during matrix impregnation and curing in unidirectional fiber beds. Compos Part A 2019;117:243–59. https://doi.org/10.1016/j.compositesa.2018.11.021.

[51] Castro J, Sket F, González C. S-XCT experimental determination of local contact angle and meniscus shape in liquid moulding of composites. Compos Sci Technol 2020;108362. https://doi.org/10.1016/j.compscitech.2020.108362.

[52] David C, Nöhammer B, Solak HH, Zielger E. Differential x-ray phase contrast imaging using a shearing interferometer. Appl Phys Lett 2002;81:3287–9. https://doi.org/10.1063/1.1516611.

[53] Momose A. Phase-sensitive imaging and phase tomography using X-ray interferometers. Opt Express 2003;11:2303–14. https://doi.org/10.1364/OE.11.002303.

[54] Momose A. Development toward high-resolution X-ray phase imaging. Microscopy 2017;66:155–66. https://doi.org/10.1093/jmicro/dfx013.

[55] Weitkamp T, Diaz A, David C, Pfeiffer F, Stampanoni M, Cloetens P, et al. X-ray phase imaging with a grating interferometer. Opt Express 2005;13:6296–304. https://doi.org/10.1364/OPEX.13.006296.

[56] Endrizzi M. X-ray phase-contrast imaging. Nucl Inst Methods Phys Res A 2018;878: 88–98. https://doi.org/10.1016/j.nima.2017.07.036.

[57] Pfeiffer F, Bech M, Bunk O, Kraft P, Einkenberry EF, Brönnimann C, et al. Hard-X-ray dark-field imaging using a grating interferometer. Nat Mater 2008;7:134–7. https://doi.org/10.1038/nmat2096.

[58] Kaeppler S, Kaeppler S, Rieger J, Pelzer G, Horn F, Michel T, et al. Improved reconstruction of phase- stepping data for Talbot – Lau x-ray imaging. J Med Imaging 2020;4. https://doi.org/10.1117/1.JMI.4.3.034005.

[59] Gradl R, Dierolf M, Yang L, Hehn L, Günther B, Möller W, et al. Visualizing treatment delivery and deposition in mouse lungs using in vivo x- ray imaging. J Control Release 2019;307:282–91. https://doi.org/10.1016/j.jconrel.2019.06.035.

[60] Yang F, Prade F, Griffa M, Jerjer I, Di Bella C, Herzen J, et al. Dark-field X-ray imaging of unsaturated water transport in porous materials. Appl Phys Lett 2014; 105. https://doi.org/10.1063/1.4898783.

[61] Prade F, Fischer K, Heinz D, Meyer P, Mohr J, Pfeiffer F. Time resolved X-ray Dark-Field Tomography Revealing Water Transport in a Fresh Cement Sample. Sci Rep 2016. https://doi.org/10.1038/srep29108.

[62] Le TH, Dumont PJ, Orgéas L, Favier D, Salvo L, Boller E. X-ray phase contrast microtomography for the analysis of the fibrous microstructure of SMC composites. Compos Part A Appl Sci Manuf 2007;39:91–103. https://doi.org/10.1016/j.compositesa.2007.08.027.

[63] Revol V, Plank B, Kaufmann R, Kastner J, Kottler C, Neels A. Laminate fibre structure characterisation of carbon fibre-reinforced polymers by X-ray scatter dark field imaging with a grating interferometer. NDT E Int 2013;58:64–71. https://doi.org/10.1016/j.ndteint.2013.04.012.

[64] Gresil M, Revol V, Kitsianos K, Kanderakis G. EVITA Project : Comparison Between Traditional Non-Destructive Techniques and Phase Contrast X-Ray Imaging Applied to Aerospace Carbon Fibre Reinforced Polymer. Appl Compos Mater 2017; 24:513–24. https://doi.org/10.1007/s10443-016-9540-1.

[65] Hannesschläger C, Revol V, Plank B, Salaberger D, Kastner J. Fibre structure characterisation of injection moulded short fibre-reinforced polymers by X-ray scatter dark field tomography. Case Stud Nondestruct Test Eval 2015;6:34–41. https://doi.org/10.1016/j.csndt.2015.04.001.

[66] Senck S, Plank B, Kastner J, Revol V, Dobes K, Scheerer M. Non-destructive evaluation of defects in polymer matrix composites for aerospace applications using X-ray Talbot- Lau interferometry and micro CT. Am Inst. Aeronaut Astronaut 2017. https://doi.org/10.2514/6.2017-0355.

[67] Senck S, Scheerer M, Revol V, Plank B, Hannesschläger C, Gusenbauer C, et al. Microcrack characterization in loaded CFRP laminates using quantitative two- and three-dimensional X-ray dark- field imaging. Compos Part A 2018;115:206–14. https://doi.org/10.1016/j.compositesa.2018.09.023.

[68] Gusenbauer C, Kastner J, Reiter M, Plank B, Salaberger D, Senck S. Porosity Determination of Carbon and Glass Fibre Reinforced Polymers Using Phase-Contrast Imaging. J Nondestruct Eval 2019;38:1–10. https://doi.org/10.1007/s10921-018-0529-6.

[69] Pathak AK, Yokozeki T, Imada M, Kido K. In-situ observation of tensile failure mode in cross-ply CFRP laminates using Talbot-Lau interferometry. Compos Struct 2020;253. https://doi.org/10.1016/j.compstruct.2020.112758.

[70] Shoukroun D, Massimi L, Iacoviello F, Endrizzi M, Bate D, Olivo A, et al. Enhanced composite plate impact damage detection and characterisation using X-Ray refraction and scattering contrast combined with ultrasonic imaging. Compos Part B 2020;181. https://doi.org/10.1016/j.compositesb.2019.107579.

[71] Morimoto N, Kimura K, Shirai T, Doki T, Sano S, Horiba A, et al. Talbot-Lau interferometry-based x-ray imaging system with retractable and rotatable gratings for nondestructive testing. Sci Instruments 2020;91. https://doi.org/10.1063/1.5131306.

[72] Kottler C, Revol V, Kaufmann R, Urban C. Dual energy phase contrast x-ray imaging with Talbot-Lau interferometer Dual energy phase contrast x-ray imaging with Talbot-Lau interferometer. J Appl Phys 2010;108. https://doi.org/10.1063/1.3512871.

[73] Lauridsen T, Lauridsen EM, Feidenhans R. Mapping misoriented fibers using X-ray dark field tomography. Appl Phys A 2014;741–5. https://doi.org/10.1007/s00339-014-8398-z.

[74] Kottler C, Pfeiffer F, Bunk O, Grünzweig C, Bruder J, Kaufmann R. Phase contrast X-ray imaging of large samples using an incoherent laboratory source. Phys Status Solidi 2007;204:2728–33. https://doi.org/10.1002/pssa.200675659.

[75] Caglar B, Orgéas L, Rolland S, Sozer EM, Michaud V. Permeability of textile fabrics with spherical inclusions. Compos Part A 2017;99:1–14. https://doi.org/10.1016/j.compositesa.2017.03.031.

[76] Morren G, Bottiglieri M, Bossuyt S, Sol H, Lecompte D, Verleye B, et al. A reference specimen for permeability measurements of fibrous reinforcements for RTM. Compos Part A 2009;40:244–50. https://doi.org/10.1016/j.compositesa.2008.11.011.

[77] Yashiro W, Terui Y, Kawabata K, Momose A. On the origin of visibility contrast in x-ray Talbot interferometry. Opt Express 2010;18. https://doi.org/10.1364/OE.18.016890.

[78] Revol V, Kottler C, Kaufmann R, Neels A, Dommann A. Orientation-selective X-ray dark field imaging of ordered systems. J Appl Phys 2012;112. https://doi.org/10.1063/1.4768525.

[79] Abaimov SG, Lebedev OV, Grishaev V, Gilmutdinov BN, Akhatov IS. Edge flow profile under radial injection at constant pressure: Analytical predictions vs. experiment. Compos Struct 2020;242. https://doi.org/10.1016/j.compstruct.2020.112101.

[80] Revol V, Jerjen I, Kottler C, Schu P, Kaufmann R, Lu T, et al. Sub-pixel porosity revealed by x-ray scatter dark field imaging. J Appl Phys 2011;110. https://doi.org/10.1063/1.3624592.

[81] Bech M, Bunk O, Donath T, Feidenhans R, David C, Pfeiffer F. Quantitative X-ray dark-field computed tomography. Phys Med Biol 2010;55:5529–39. https://doi.org/10.1088/0031-9155/55/18/017.

[82] Chabior M, Donath T, David C, Schuster M, Schroer C, Pfeiffer F. Signal-to-noise ratio in x ray dark-field imaging using a grating interferometer. J Appl Phys 2011; 110. https://doi.org/10.1063/1.3630051.

[83] Revol V. X-ray phase contrast imaging by grating interferometry. University of Zurich; 2011.

[84] Bico J, Quéré D. Precursors of impregnation. Europhys Lett 2003;61(3):348–53. https://doi.org/10.1209/epl/i2003-00196-9.

[85] Berger MJ, Hubbell JH, Seltzer SM, Chang J, Coursey JS, Sukumar R, et al. XCOM: Photon Cross Sections Database. n.d.

[86] Russian Academy of Sciences. Institute of Microelectronics Technology. X-ray Optics Calculator n.d. http://purple.ipmt-hpm.ac.ru/xcalc/xcalc_mysql/ref_index.php.